Emerging spintronic and valleytronic phenomena in noncentrosymmetric variants of the Kane-Mele $X_4Y_2Z_6$ materials family (X = Pt, Pd, Ni; Y = Hg, Zn, Cd; Z = S, Se, Te)

Majeed Ur Rehman,[1,2,*] Zia Ur Rahman,[3] and Maryam Kiani[4]

[1]*Songshan Lake Materials Laboratory, Dongguan, Guangdong 523808, China*

[2]*Institute of Physics, Chinese Academy of Sciences, Beijing 100190, China*

[3]*Shenzhen Key Laboratory of Advanced Thin Films and Applications, Key Laboratory of Optoelectronic Devices and Systems of Ministry of Education and Guangdong Province, College of Physics and Optoelectronic Engineering, Shenzhen University, Shenzhen, Guangdong 518060, China*

[4]*College of Physics and Optoelectronic Engineering, Shenzhen University, Shenzhen, Guangdong 518060, China*

(Received 20 September 2023; accepted 6 February 2024; published 15 April 2024)

The realization of the Kane-Mele model in Xene solids faces challenges due to weak spin-orbit coupling (SOC). Nevertheless, the recently discovered $X_4Y_2Z_6$ family (X=Pt, Pd, Ni; Y=Hg, Zn, Cd; and Z=S, Se, Te) offers a promising opportunity with larger SOC. However, the presence of centrosymmetry in this family hinders the achievement of several cross-coupling phenomena based on spintronics and valleytronics. This study explores a noncentrosymmetric version of the Kane-Mele family, $X_4YY'Z_6$ and $X_4YY'(ZZ')_3$, comprising over 16 experimentally accessible members. The results reveal intertwined phenomena involving topology, spin, and valley degrees of freedom, including the quantum valley/spin Hall effect, spin-valley locking, and spin-valley selective optical transitions. Additionally, Rashba coupling coexists with Ising spin splitting, enabling valley spin valve functionality and out-of-plane spontaneous electric polarization. Quantum valley Hall kink states can be achieved on the domain walls between these noncentrosymmetric monolayers due to opposite spin-valley Berry curvatures. External factors, like electric fields and strain, induce various topological phase transitions. This study lays the foundation for exploring spin-valley physics in low-dimensional topological materials with noncentrosymmetry.

DOI: 10.1103/PhysRevB.109.165424

I. INTRODUCTION

Spin and valley indices are important degrees of freedom for next-generation information storage and processing [1–5]. However, in most two-dimensional (2D) materials, such as topological valleytronic solids, these degrees of freedom are uncoupled, preventing the use of useful features based on spin-valley locking. In order to couple these degrees of freedom and introduce phenomena based on their joint coupling, exploitation of centrosymmetry is required. So far, various efforts have been made to predict materials that can combine and couple spintronics and valleytronics-based applications. In this context, Xene solids, including graphene [6], germanene, and stanene, have received considerable attention because they offer a platform for the manipulation of spin and valley degrees of freedom [7–14]. However, the weak spin-orbit coupling (SOC) effects and centrosymmetric nature of Xene solids limit their usefulness for certain phenomena. Researchers have discovered some new families of 2D materials with broken inversion symmetry, such as gapped graphene and transition metal dichalcogenides (TMDCs), which offer a better platform for manipulating spin- and valley-dependent properties, making them highly desirable for spintronic and valleytronic applications [15–19].

The Kane-Mele model is a theoretical framework that incorporates both spin and valley degrees of freedom to explain the topological behavior of Xene solids [20]. However, practical implementation of this model in Xene solids has been challenging due to insufficient SOC effects. Many efforts have been made to improve the SOC effects in this family using various external proximity means, but it remains difficult to realize the Kane-Mele model in Xene materials. Recently, a new family of materials ($X_4Y_2Z_6$) was experimentally synthesized, offering renewed hope for the practical realization of the Kane-Mele model [21–25]. In the $X_4Y_2Z_6$ family, X=Pt, Pd, or Ni; Y=Hg, Zn, or Cd; and Z=S, Se, or Te. Within this family, two members, $Pt_4Hg_2Se_6$ and $Pd_4Hg_2Se_6$, have been found to exhibit quantum spin Hall features with a large nontrivial band gap [21,25]. The $X_4Y_2Z_6$ family follows the Kane-Mele model, which is also used to describe Xene solids, but at a considerably larger energy scale [25]. The $X_4Y_2Z_6$ family is composed of ternary materials that differ from the Xene family in many ways. However, the Y lattice in this family forms a buckled-type honeycomb structure, making it an alternative to the Xene family in the context of spintronics and valleytronics. This family could provide a better platform for achieving the Kane-Mele model and is therefore a promising avenue for research in the field of topological materials.

In contrast to the Xene family, the $X_4Y_2Z_6$ family exhibits SOC at a much larger scale, making it interesting and suitable for spin- and valley-related practical applications [26]. Two members of this family, $Pt_4Hg_2Se_6$ and $Pd_4Hg_2Se_6$,

*Corresponding author: majeedqau@live.com

have already been experimentally synthesized. The effects of time-reversal symmetry breaking have been studied by growing this family over magnetic substrates to explore the valley-polarized quantum anomalous Hall effect [27,28]. In a recent study, it was discovered that exposing the $X_4Y_2Z_6$ family to a vertical electric field can lead to the coexistence of spin-valley Hall effects [26].

However, there are still many phenomena that have not yet been observed in the $X_4Y_2Z_6$ family, despite its potential for various applications. These phenomena are based on the principle of breaking centrosymmetry and include spin-valley locking, spontaneous polarization, Rashba and Ising spin splitting, and quantum spin-valley Hall features. A comprehensive study is needed to break the centrosymmetry and explore the aforementioned spin-valley-based hallmarks in this family. This type of study is critical as it may lead to the discovery of a range of phenomena, including the quantum valley Hall effect, Rashba spin splitting, the spin-valley Hall effect, and valley-spin-dependent optical absorption. It could also establish a platform where the integration of topological spintronics and valleytronics can be realized, potentially leading to the discovery of several interesting phenomena. For instance, the coexistence of spin-valley Hall effects and Rashba and valley Zeeman-type spin splitting may be observed in this family, which could pave the way for advanced technologies with a range of applications. By exploring broken centrosymmetry in the $X_4Y_2Z_6$ family, researchers may be able to identify novel materials that exhibit these phenomena, leading to the development of faster and more efficient computing systems.

In this paper, going one step forward, we present a recent development in the study of the Kane-Mele $X_4Y_2Z_6$ family. Specifically, we introduce a noncentrosymmetric version of this family that allows for the presence of spin-valley coupling. To achieve this, we use asymmetrical structural modification, which is a promising method for exploiting centrosymmetry and inducing staggered potential U in this newly synthesized Kane-Mele family. Staggered potential U typically refers to a potential energy landscape in a system where there is an alternation or staggering of potential values. This term is commonly used in condensed matter physics, particularly in the context of lattice structures or electronic systems. Overall, we predicted more than 16 stable noncentrosymmetric Kane-Mele monolayers.

In the proposed monolayers, we have successfully combined strong SOC, valley properties, noncentrosymmetry, and topology. This represents a significant advancement in our understanding of this family and has important implications for the field of spintronics and valleytronics. By incorporating these key ingredients on the same platform, we have created a unique opportunity to explore a range of phenomena, including quantum valley Hall effects, Rashba spin splitting, and spin-valley Hall effects. Through an extensive search, we predicted more than 16 stable noncentrosymmetric Jacutingaite monolayers.

In this work, calculations are carried out using an analytical low-energy $k \cdot p$ model and the first-principles approach as implemented in the Vienna Ab initio Simulation Package (VASP) [29,30]. Topological properties such as Berry curvatures $\Psi_z(k)$, the topological $\mathcal{Z}_2$ invariant, and surface states are calculated using the algorithm discussed in Refs. [31–33]. Simulation methods are described in more detail in the Supplemental Material (SM) [34].

II. CONTINUUM MODEL

To better understand the emergence of noncentrosymmetry in the $X_4Y_2Z_6$ family, we begin by using a low-energy continuum model that focuses on the valley points. This model effectively explains the underlying physics. Structural engineering using asymmetrical modification introduces two new terms to the Hamiltonian: the staggered potential U and the Rashba SOC (RSOC). The low-energy $k \cdot p$ Hamiltonian for $Pt_4Hg_2Se_6$ near the valley points K and K' can be expressed as follows [35–37]:

$$H = \hbar v_F(\eta\sigma_x k_x + \sigma_y k_y)\mathbf{1}_s + \eta\lambda_{\rm so} s_z\sigma_z + \lambda_R(\eta\sigma_x s_y - \sigma_y s_x) + U\sigma_z\mathbf{1}_s. \quad (1)$$

Here, $\sigma_{x,y,z}$ and $s_{x,y,z}$ are Pauli matrices in the sublattice pseudospin and real spin spaces, respectively, and $\mathbf{1}_s$ denotes the identity matrix in the spin space. The valley index η takes values of either $+1$ or -1, representing the two valleys K and K'. The first term in Eq. (1) corresponds to the massless kinetic hopping term (similar to the graphene system). The second term represents the Kane-Mele SOC with $\lambda_{\rm so} \sim 81.2$ meV [25]. It is 4 orders of magnitude larger than the SOC in graphene and respects both time-reversal ($\mathcal{T}$) and space-inversion ($\mathcal{P}$) symmetries. The third is the Rashba SOC λ_R arising due to a perpendicular electric field or structural asymmetry. The fourth term arises due to a staggered sublattice potential U, breaking inversion symmetry and lifting spin degeneracy. In graphene and similar systems, a sublattice staggered potential is an energy difference between sublattices (A and B), impacting various phenomena such as the band gap opening and topologically nontrivial states. The fourth and fifth terms survive only when the $\mathcal{P}$ symmetry is broken in the system. We first diagonalize this Hamiltonian for the case of $\lambda_R = 0$ and then take the case of $\lambda_R \neq 0$.

A. Case of $\lambda_R = 0$

By diagonalizing the Hamiltonian (1) in the absence of Rashba SOC, we obtain the dispersion relation

$$E_{\pm s_z}(k) = \pm\sqrt{(U + \eta s_z\lambda_{\rm so})^2 + (\hbar v_F k)^2}, \quad (2)$$

where $\pm$ corresponds to conduction (+) and valence (−) bands, respectively. From the energy expression, it can be seen that the band gap [i.e., $E_g = (\eta s_z\lambda_{\rm so} + U)$] size decreases as the strength of U approaching as $\lambda_{\rm so}$ and finally closes when $U = \lambda_{\rm so}$ and reopens when $U > \lambda_{\rm so}$. This band gap closing and reopening reflect a topological phase transition from the quantum spin Hall (QSH) phase to a quantum valley Hall (QVH) phase. Further, by using the Kobu formalism [37,38], we evaluate the Berry curvature and Chern number:

$$\Omega_n^{\eta s_z}(k) = \frac{\eta\hbar^2 v_F^2(\eta s_z\lambda_{\rm so} + U)}{2[(\eta s_z\lambda_{\rm so} + U)^2 + (\hbar v_F k)^2]^{3/2}}, \quad (3)$$

$$C_\eta^{s_z} = (\eta/2)sgn[\eta s_z\lambda_{\rm so} + U]. \quad (4)$$

When $U = 0$, we find that $\mathcal{C}_\uparrow = \mathcal{C}_K^\uparrow + \mathcal{C}_{K'}^\uparrow = 1$ and $\mathcal{C}_\downarrow = \mathcal{C}_K^\downarrow + \mathcal{C}_{K'}^\downarrow = -1$. This leads to a Chern number $\mathcal{C} = 0$, spin Chern number $\mathcal{C}_s[\equiv (\mathcal{C}_\uparrow - \mathcal{C}_\downarrow)/2] = 1$, and valley Chern number $\mathcal{C}_v[\equiv (\mathcal{C}_K - \mathcal{C}_{K'})/2] = 0$. Thus, when $U = 0$ (as in the case of $Pt_4Hg_2Se_6$), the system remains in the QSH state, which is completely consistent with our first-principles calculations (see below). Now by increasing U from zero the system remains in the QSH state as long as $U < \lambda_{so}$. However, when $U > \lambda_{so}$, the system makes a phase transition from the QSH state ($\mathcal{C}_s = 1$) to a QVH state ($\mathcal{C}_v = 1$). Thus, the topological states in $Pt_4Hg_2Se_6$ can be controlled through the interplay of the staggered potential U and SOC strength.

When the Fermi level lies in the band gap, the Hall conductivity for each spin takes the form

$$\sigma_{xy}^{s_z} = \pm(e^2/2h) \sum_{\eta=\pm} \frac{(\eta\lambda_{so} \pm U)}{\sqrt{(\eta\lambda_{so} \pm U)^2 + (\hbar v_F k_F)^2}}, \quad (5)$$

where the $+$ $(-)$ sign corresponds to spin up (spin down). Similarly, we find the Hall conductivity for each valley:

$$\sigma_{xy}^{\eta} = \pm(e^2/2h) \sum_{\eta=\pm} \frac{\pm\lambda_{so} s_z + U}{\sqrt{(\pm\lambda_{so} s_z + U)^2 + (\hbar v_F k_F)^2}}, \quad (6)$$

where the $+$ $(-)$ sign corresponds to K (K').

B. Case of $\lambda_R \neq 0$

We numerically diagonalized the Hamiltonian (1) in the presence of Rashba interaction. In the presence of RSOC, we split our analysis into the (1) $\lambda_R < \lambda_{so}$ and (2) $\lambda_R > \lambda_{so}$ cases. For the case of $\lambda_R < \lambda_{so}$, the results are almost similar to the case of $\lambda_R \approx 0$, as shown in Figs. 1(d)–1(f). For instance, for $U \preccurlyeq \lambda_R$, the system remains in the QSH regime. The band gap vanishes at $U = \lambda_{so}$ (i.e., semimetallic state) and switches to QVH when $U > \lambda_{so}$. For the $\lambda_R > \lambda_{so}$ case the situation is completely different. As can be seen from Figs. 1(g)–1(i), when the strength of U is comparable to λ_R (i.e., $U = \lambda_R$), the massless Dirac points shift away from the K and K' points to some nearby finite momentum Q. After the strength of U is increased further, the band gap opens around theses avoided band crossing points, and the system finally switches to the QVH insulating phase. For a clear demonstration, a topological phase diagram as a function of U and λ_R in the presence of finite Kane-Mele SOC ($\lambda_{so} \sim 81.2$ meV) is shown in Fig. 1(j), where the all topological phases are highlighted.

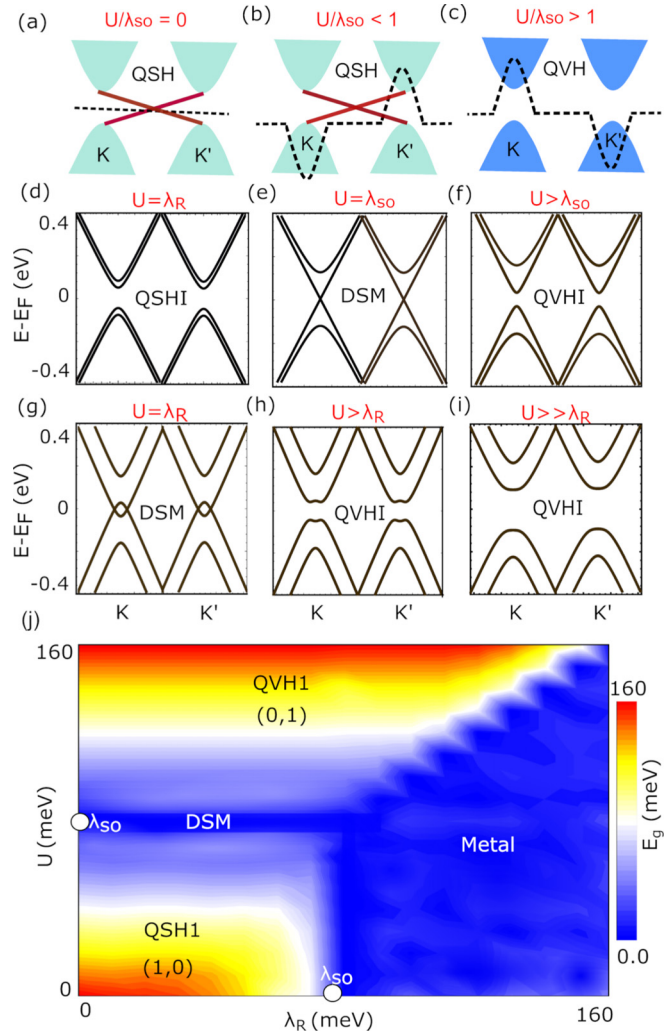

FIG. 1. Continuum model: (a)–(c) Schematic representation illustrating the evolution of Berry curvature and the topological phase transition for different strengths of U and λ_{so} in the $X_4Y_2Z_6$ family. (d)–(f) Interplay between λ_{so} and U under the condition $\lambda_{so} > \lambda_R$. (g)–(i) Same as (d)–(f), but for the case $\lambda_{so} < \lambda_R$. QSHI, QVHI, and DSM represent the states of the quantum spin Hall insulator, quantum valley Hall insulator, and Dirac semimetal, respectively. (j) Topological phase diagram as a function of U and λ_R in the presence of Kane-Mele SOC $\lambda_{so} \sim 81.2$ meV. The spin and valley Chern numbers ($\mathcal{C}_s$, $\mathcal{C}_v$) are also labeled.

III. MATERIAL DESIGN

We explore the interplay between SOC and the staggered potential difference U in real materials systems by introducing a breaking of centrosymmetry in the Kane-Mele $X_4Y_2Z_6$ family of materials. The centrosymmetric $X_4Y_2Z_6$ family consists of five atomic layers covalently bonded along the z axis in the sequence of Z-Y-X-Y-Z [see Fig. 1(a)]. The noncentrosymmetric version of the Kane-Mele $X_4Y_2Z_6$ family can be described by the formulas $X_4YY'Z_6$ and $X_4Y_2(ZZ')_3$ when an asymmetrical-type modification is performed on the Y and Z lattices, respectively (see Fig. 1 for structural composition). This modification breaks the inversion symmetry and induces a staggered-type potential U that competes with the Kane-Mele SOC. We refer to this modification as asymmetrical-type transformation, which reduces the point group of the $X_4Y_2Z_6$ family from centrosymmetric D_{3d} to noncentrosymmetric C_{3v}. This asymmetrical-type modification induces an out-of-plane spontaneous polarization P_s due to the noncentrosymmetric geometry. While, in principle, there are numerous atom types suitable for substitution, our approach focuses specifically on Janus-type structural engineering to break centrosymmetry. In Janus-type structural engineering, one sublayer in the material is entirely replaced by another within the same group. This method has been successfully applied to the TMDC family and experimentally realized in PtSSe, MoSSe, and MoSH Janus systems [39–42]. The Janus-type structural modification allows for various spin-valley-based

TABLE I. Relaxed structural geometry, including equilibrium lattice parameters ($a = b$), layer thickness l_z, measured spontaneous polarization P_s, electrical transport energy gaps E_g, cohesive energies E_{coh}, Ising spin splitting size, and the corresponding topological states in our proposed noncentrosymmetric Kane-Male $X_4YY'Z_6/X_4Y_2(ZZ')_3$ family. QVHS and SVHS represent the quantum valley Hall state and spin-valley Hall state, respectively.

Serial No.	System	Lattice constant (Å)	Thickness l_z (Å)	E_g (meV)	E_{coh} (meV)	Polarization (pC m^{-1})	Ising splitting (meV)	Topological state
1	$Pt_4Hg_2(SSe)_3$	7.356	3.72	285	3.962	0.15	167	QVHS and SVHS
2	$Pt_4Hg_2(STe)_3$	7.579	3.58	159	3.83	4.3	184	QVHS and SVHS
3	$Pt_4Hg_2(SeTe)_3$	7.745	3.38	158	3.72	2.6	195	QVHS and SVHS
4	$Pt_4HgCdSe_6$	7.521	3.57	688	3.92	4.8	154	QVHS and SVHS
5	$Pt_4HgZnSe_6$	7.524	3.47	892	3.97	0.9	217	QVHS and SVHS
6	$Pd_4Hg_2(SSe)_3$	7.273	3.83	138	3.27	0.1	76	QVHS and SVHS
7	$Pd_4Hg_2(STe)_3$	7.529	3.82	−181	3.16	3.5	127	SVHS
8	$Pd_4Hg_2(SeTe)_3$	7.693	3.48	−18	3.058	2.64	119	SVHS
9	$Pd_4HgCdSe_6$	7.462	3.63	452	3.24	3.87	83	QVHS and SVHS
10	$Pd_4HgZnSe_6$	7.507	3.65	742	3.28	0.22	80	QVHS and SVHS
11	$Ni_4Hg_2(SSe)_3$	6.972	4.81	−20	3.66	2.68	63	SVHS
12	$Ni_4Hg_2(STe)_3$	7.225	4.29	3	3.53	2.17	109	QVHS and SVHS
13	$Ni_4Hg_2(SeTe)_3$	7.438	3.96	12.5	3.38	0.3	127	QVHS and SVHS
14	$Ni_4HgCdSe_6$	7.208	3.58	280	3.58	3.96	57	QVHS and SVHS
15	$Ni_4HgZnSe_6$	7.226	3.42	435	3.62	0.35	55	QVHS and SVHS
16	$(PtPd)_2Hg_2Se_6$	7.488	3.55	−48	3.49	0	0	Topological semimetals
17	$(PtNi)_2Hg_2Se_6$	7.278	3.488	−15	3.66	0	0	Topological semimetals

phenomena, such as the quantum spin/valley Hall effect, spin-valley coupling, spin-valley-dependent optical interband transition, spin-polarized trigonal warping effects, and valley-contrasting Berry curvature behavior. We also replaced the half-centric Pt layer with Pd or Ni atomic layers in the $Pt_4Hg_2Se_6$ system to form layers like $(PtPd)_2Y_2Z_6$ and $(PtNi)_2Y_2Z_6$. However, this type of chemical modification preserves the centrosymmetry in the parent structure, thereby precluding the spin splitting and valley-contrasting Berry curvature behavior.

Overall, we predicted more than 16 stable noncentrosymmetric monolayers and summarize their geometrical parameters such as the lattice constants, thickness, buckling distance of the Hg lattice, and vertical distance from the centric M layer in Table I.

To ensure the experimental feasibility of synthesizing our proposed noncentrosymmetric Kane-Male $X_4YY'Z_6/X_4Y_2(ZZ')_3$ family, we assessed their stability using various methodologies. The phonon band structures of these proposed monolayers do not show any free soft modes (see Fig. 2). Moreover, molecular dynamics simulations at room temperature show smooth energy fluctuations, further supporting their stability. The cohesive energy spectrum of these monolayers falls within the range of other 2D materials that have already been experimentally synthesized (see Table I). Taken together, these results suggest that the noncentrosymmetric $X_4YY'Z_6/X_4Y_2(ZZ')_3$ family can be synthesized experimentally, and its unique properties make its members promising candidates for exploring spin-valley-based phenomena such as the quantum spin/valley Hall effect, spin-valley coupling, spin-valley-dependent optical interband transition, spin-polarized trigonal warping effects, and valley-contrasting Berry curvature behavior.

IV. SPONTANEOUS ELECTRIC POLARIZATION

The centrosymmetric version of the Kane-Mele family (i.e., $X_4Y_2Z_6$) lacks spontaneous polarization, while the noncentrosymmetric version, $X_4YY'Z_6/X_4Y_2(ZZ')_3$, exhibits spontaneous polarization due to broken centrosymmetry. The phenomenon of spontaneous polarization was examined by determining the out-of-plane electric polarization. The results indicate that substantial magnitudes of electric polarization were observed in the noncentrosymmetric $X_4YY'Z_6/X_4Y_2(ZZ')_3$ Kane-Mele family (see Table I).

The induced polarization in these noncentrosymmetric monolayers is due to the inhomogeneous charge distribution, which is illustrated in Figs. 3(e)–3(h). The polarization strength varies depending on the electronegativity difference in each lattice. For instance, the polarization strength is higher in $Pt_4Hg_2(STe)_3$ compared to $Pt_4Hg_2(SeTe)_3$ (see Table I). Similarly, $Pt_4HgZnSe_3$ has a higher polarization strength than $Pt_4HgCdSe_3$ (see Table I). The differences in polarization strength can be attributed to the different chemical compositions of these monolayers. Also, the electronegativity difference is a crucial factor in determining the strength of polarization in these noncentrosymmetric monolayers. Similarly, the strength of polarization is higher in the Pt-based monolayers compared to Pd and Ni-based monolayers (see Table I).

V. SPIN-VALLEY COUPLING AND TOPOLOGICAL PHASE TRANSITION

Figure 4 shows the electronic band structures of the $X_4YY'Z_6/X_4Y_2(ZZ')_3$ monolayers. We observed significant changes in the non-SOC band structure as a result of the structural modifications made to the $X_4Y_2Z_6$ family (see

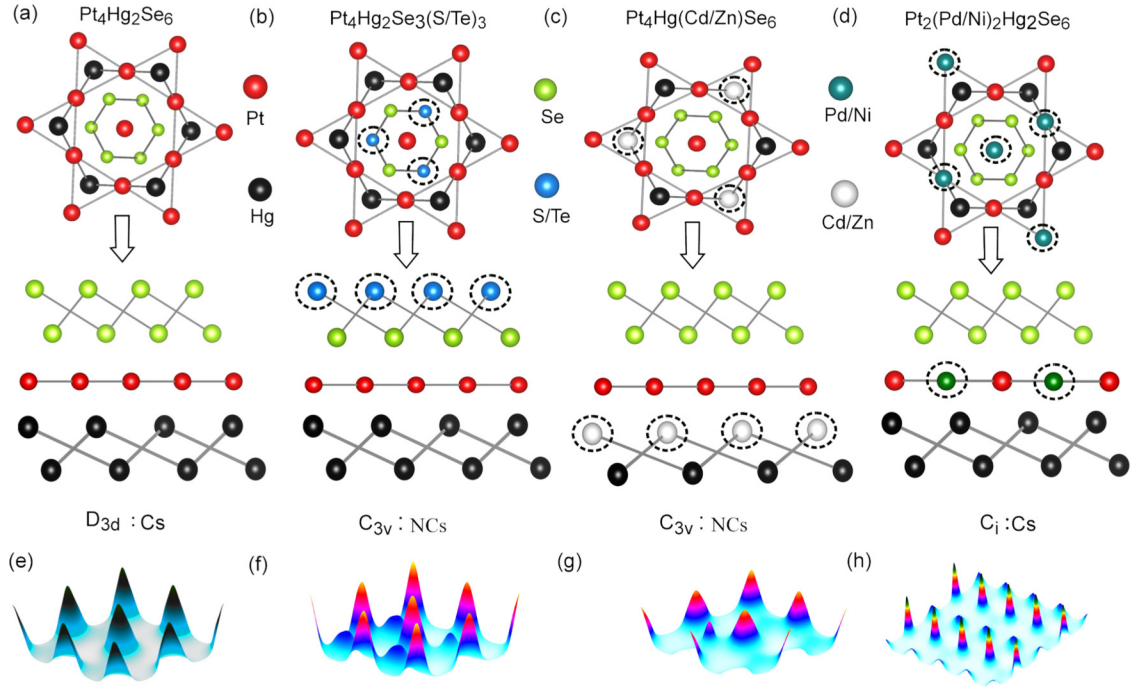

FIG. 2. Exploiting centrosymmetry in the Kane-Mele $X_4Y_2Z_6$ family: Crystal structures of (a) $Pt_4Hg_2Se_6$, (b) $Pt_4Hg_2Se_3(S/Te)_3$, (c) $Pt_4Hg(Cd/Zn)Se_6$, and (d) $Pt_2(Pd/Ni)_2Hg_2Se_6$. The corresponding point groups are also displayed, where Cs (NCs) denotes centrosymmetry (noncentrosymmetry). (e)–(h) The corresponding charge density profiles. The homogeneity and inhomogeneity in the charge density profile can be observed in (e) and (h) and (f) and (g), reflecting the existence and nonexistence of centrosymmetry, respectively.

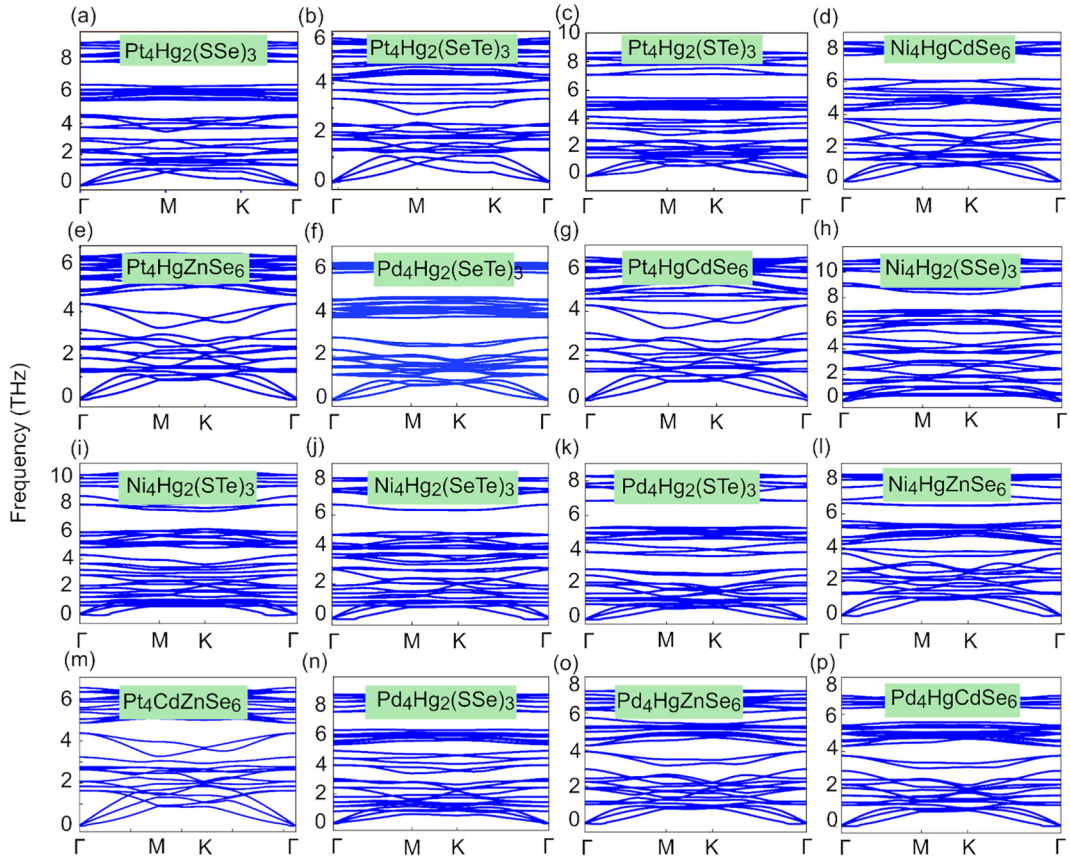

FIG. 3. The phonon band dispersion of various noncentrosymmetric Kane-Male $X_4YY'Z_6/X_4Y_2(ZZ')_3$ monolayers, demonstrating the absence of soft modes. The absence of soft modes signifies both the dynamic stability and experimental accessibility of the proposed monolayers.

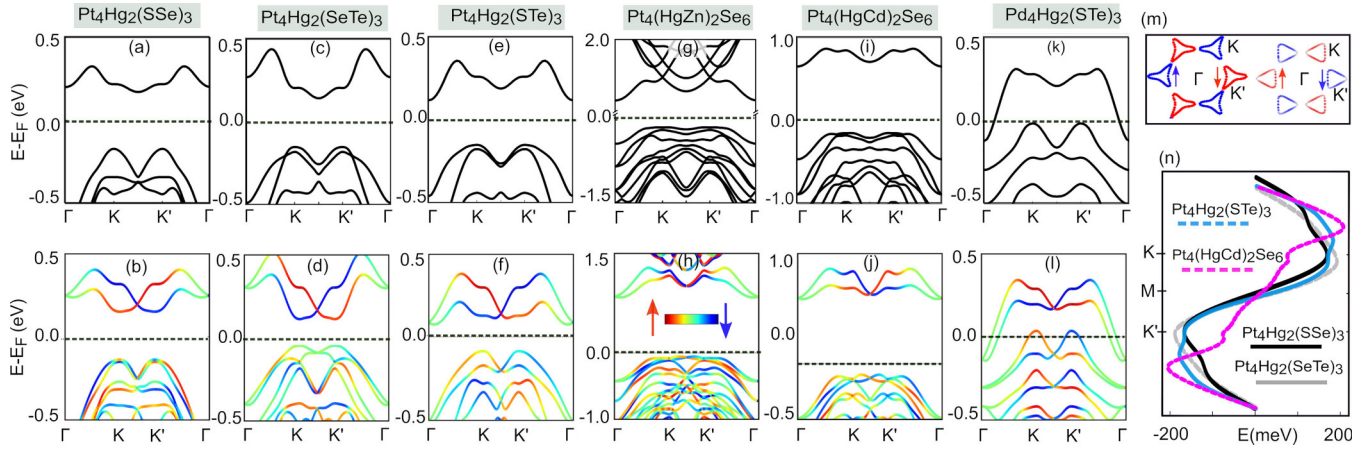

FIG. 4. (a), (c), (e), (g), (i), and (k) Non-SOC and (b), (d), (f), (h), (j), and (l) the corresponding SOC-included S_z-resolved energy spectrum for various noncentrosymmetric Kane-Male $X_4YY'Z_6/X_4Y_2(ZZ')_3$ monolayers. The valley-dependent spin polarization is evident. (m) Constant energy contour maps calculated for the top valence bands (right) and the lower conduction bands (left). The triangular and starlike contours reflect the high trigonal distortion around the Fermi level in these proposed monolayers. (n) The size of the momentum-dependent spin splitting in the top valence and lower conduction bands in our proposed monolayers.

Fig. 4). Specifically, we noted the following changes: (1) The presence of staggered structural engineering caused the disintegration of the massless Dirac spectrum around valley points, leading to a semimetallic behavior. This change indicates the breaking of centrosymmetry and the intervention of a staggered-type potential U. (2) The strength of U varied depending on the modification type and electronegativity difference within the monolayers. For example, the U strength was higher in the case of asymmetrical modification on the Hg lattice compared to the Se lattice in the $Pt_4Hg_2Se_6$ layer. Moreover, the U value is higher for $Pt_4Hg_2(STe)_3$ compared to $Pt_4Hg_2(SeTe)_3$. (3) The band structures and band gaps were strongly influenced by the type of modification and electronegativity difference present in these monolayers.

When the SOC effect was activated, several observations were made. First, the size of the global band gap decreased, indicating competition between SOC and U that is directly proportional to $(\lambda_{so} - U)$. Second, the magnitude and nature of the global band gap (either direct or indirect) depended on the type of structural modification and the strength of the induced U. For example, the $Pt_4Hg_2(SeTe)_3$ and $Pt_4Hg_2(SSe)_3$ monolayers showed a direct band gap, while the $Pt_4Hg_2(STe)_3$ monolayer showed an indirect band gap. Third, opposite spin splitting of the bands was observed in valleys K and K' due to structural asymmetry. These findings indicate that the SOC effect significantly affects the electronic properties of the materials being investigated.

These monolayers exhibit valley-dependent spin splitting [see Fig. 4(n)], known as spin-valley coupling, due to their noncentrosymmetric polar nature and large SOC effects. This functionality is crucial for the realization of the coexistence of the spin-valley Hall effect. The magnitude of spin splitting varies depending on the type of structural modification (whether it is in the Se lattice or Hg lattice). For instance, the spin splitting in the lower conduction band of $Pt_4Hg_2(SeTe)_3$ reaches a sizable value of ∼200 meV, which is significantly greater than the spin splitting observed in the conduction bands of the TMDC family. Through the calculation of the Z_2 topological invariant and surface states, we realized that Pt-based (i.e., $Pt_4Y_2Z_6$) monolayers undergo a phase transition from a nontrivial QSH insulating phase ($Z_2 = 1$) to a trivial band insulator ($Z_2 = 0$) after asymmetrical structural engineering (see Fig. 4 and Table I). This phase transition arises from the higher value of the staggering potential U in comparison to the strength of SOC (see Fig. 1). However, these noncentrosymmetric Kane-Mele monolayers still possess topological significance due to their unique valley behavior. Indeed, they are QVH insulators with nonzero valley Chern numbers (see Fig. 5). The Berry curvature is predominantly located around the valley points, with opposite peaks in both valleys, which results in the spin and valley Hall effects (see Fig. 5). This phenomenon is absent in the centrosymmetric $X_4Y_2Z_6$ Kane-Mele family. The opposite Berry curvatures originating from valleys K and K' in these monolayers make them useful for applications in valleytronics and optoelectronics (see Fig. 5).

VI. VALLEY-SPIN-DEPENDENT OPTICAL SELECTION RULE

The interaction of noncentrosymmetry and strong SOC leads to the dependence of the optical selection rule on the spin and valley indices. In order to evaluate the optical interband transition induced by circularly polarized light, the spin-dependent circular polarization degree between the top valence band V_{tvb} and the lower conduction band C_{lcb}, denoted by $\eta^{(s)}(k)$, is computed. This quantity is given by $\eta^{(s)}(k) = (1/N)|P_+^{(s)}(k)| - |P_-^{(s)}(k)|^2$, where $N = |P_+^{(s)}(k)| + |P_-^{(s)}(k)|^2$. Here, $P_\pm^{(s)}(k)$ represent the interband matrix elements for the left $(-)$ and right $(+)$ circularly polarized light at a given spin s and k. They are defined as $P_\pm^{(s)}(k; n, n') = \langle n'k, s|p_x \pm ip_y|nk, s\rangle$, where n and n' represent the bands involved in the transition process and the optical processes do not involve spin-flip transitions.

Figure 5 demonstrates that our proposed noncentrosymmetric monolayers exhibit perfect circular dichroism near the valley points K and K', where the selectivity depends on the valley and decreases as one moves away from the

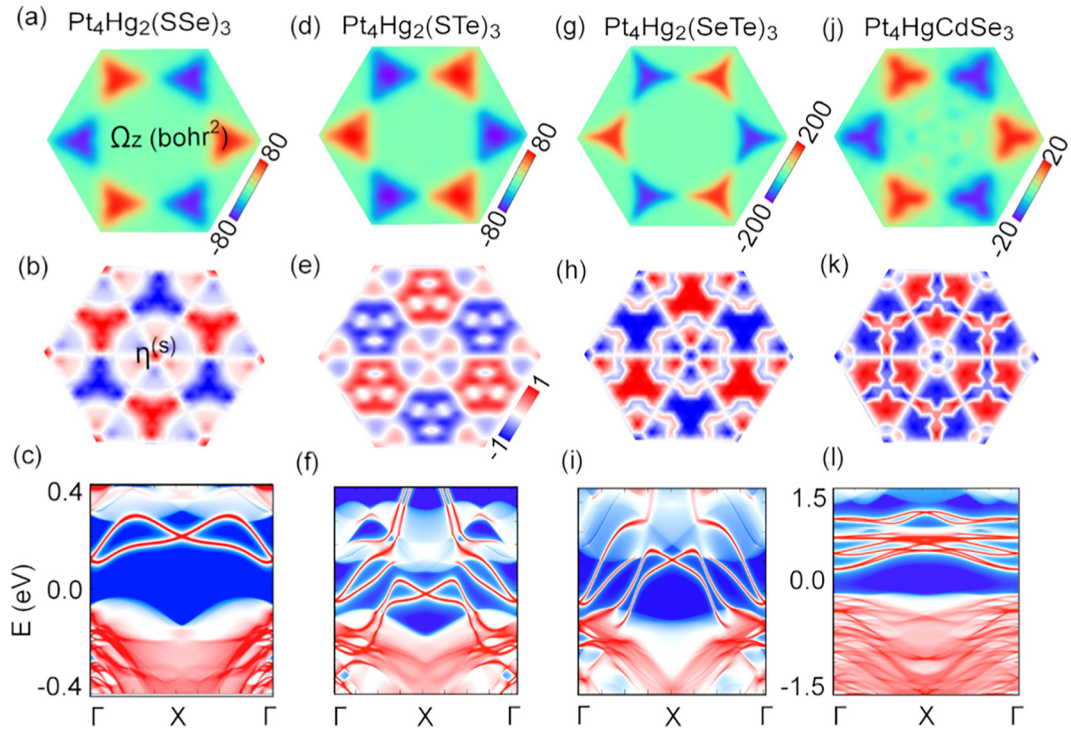

FIG. 5. Top: Berry curvature profiles in momentum space for various Kane-Male $Pt_4YY'Z_6$ monolayers, with opposite Berry curvatures in valleys K and K', signifying the quantum valley Hall effect. Middle: Corresponding circular dichroism profiles, indicating valley-dependent selective optical band transitions and signifying valley selective optical conductivity. Bottom: Corresponding surface state profiles.

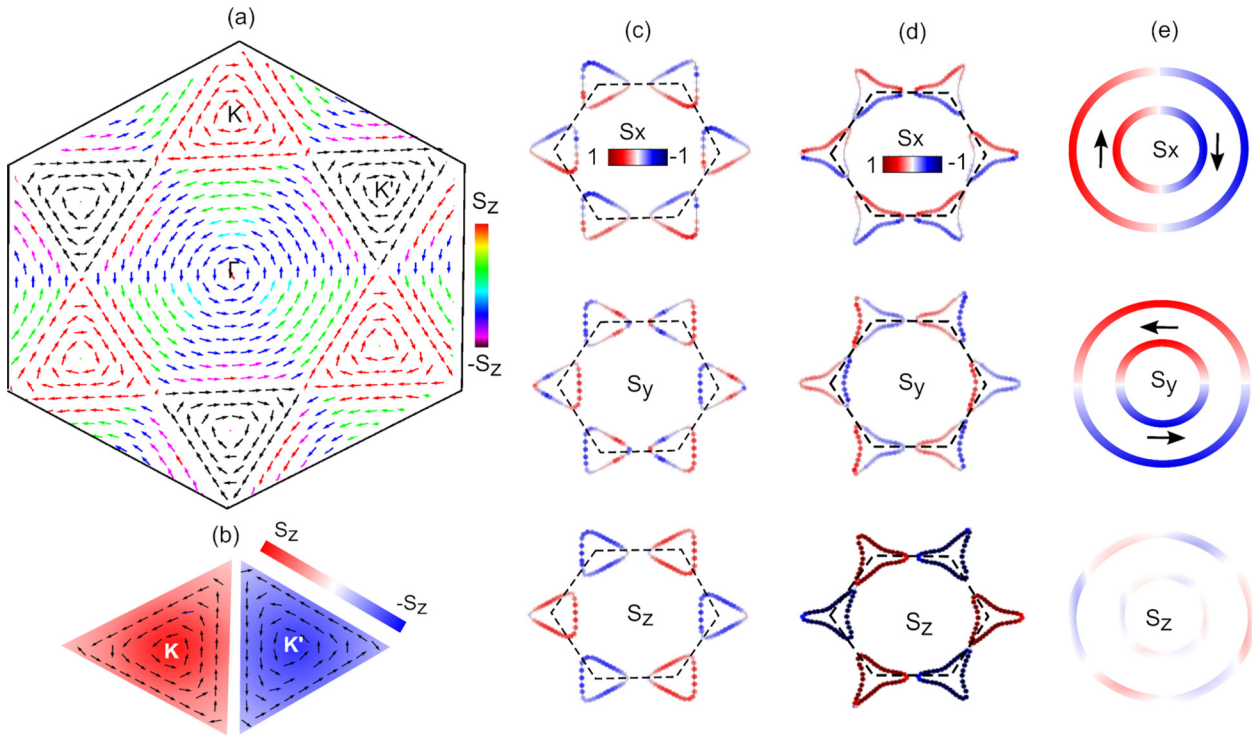

FIG. 6. (a) and (b) Spin-texture distribution over the momentum space for the $Pt_4Hg_2(SeTe)_3$ monolayer. Opposite S_z-resolved spin textures in valleys K and K' can be noticed. S_x, S_y, and S_z spin-resolved constant energy contour profiles at (c) the top valence bands and (d) the lower conduction bands for the $Pt_4Hg_2(SeTe)_3$ layer. (e) S_x-, S_y-, and S_z-resolved constant-energy contour maps at the bottom of the lower conduction band for the $Pt_4Hg_2(STe)_3$ layer. The dominant contribution of the in-plane spin component (S_x, S_y) signifies the presence of Rashba-type spin splitting around the Γ point.

valley points. Specifically, right-handed circularly polarized light excites the K valley with spin up, while the opposite valley (K') remains inactive in the optical transition. Similarly, exposing these proposed monolayers to left-handed circularly polarized light can activate the K' valley. Therefore, by controlling the light polarity, the optical transition between V_{tvb} and C_{lcb} can be selectively activated or suppressed, allowing for the valley-dependent interaction of carriers with circularly polarized light. As a result, exposing our proposed noncentrosymmetric $Pt_4Y_2Z_6$ family to circularly polarized light can selectively guide carriers from different valleys, thanks to the valley-contrasting Berry curvature behavior in these monolayers. Due to similarities in band structures, especially around the valley K and K' points, to the TMDC family, the $X_4YY'Z_6/X_4Y_2(ZZ')_3$ monolayers exhibit the same selection rules as the TMDC family.

VII. COEXISTENCE OF RASHBA AND ISING SPIN SPLITTINGS

Our proposed noncentrosymmetric monolayers $X_4YY'Z_6/X_4Y_2(ZZ')_3$ exhibit two distinct types of spin splitting, as shown in Fig. 6. Specifically, the results in Fig. 6 reveal that the spin splitting in the valence bands at the K and K' points is primarily of the Ising type, while the spin splitting in the conduction band at the Γ point is predominantly of the Rashba type with strength equal to 0.96 eV/Å in $Pt_4Hg_2(TeS)_3$. The Rashba-type spin splitting results in spins being polarized within the plane of the sample, while the Ising-type spin splitting causes spins to be polarized out of the plane of the sample. When the Ising-type spin splitting is opposite in the K and K' valleys, it is referred to as valley Zeeman spin splitting. Figure 6 illustrates the opposite spin splittings in the K and K' valleys, providing evidence of the existence of valley Zeeman spin splitting in our proposed monolayers. The simultaneous presence of spin-valley locking and Rashba-type spin splitting is observable only within the Janus family of transition metal dichalcogenides, specifically in MoSSe so far; this study demonstrates the coexistence of these phenomena in a wider range of materials.

In the $(Pd/Ni)_4Hg_2(STe)_6$ monolayers, an interesting phenomenon occurs where the Fermi level crosses both the valence band at the K and K' points and the conduction band at the Γ point simultaneously. Since the Berry curvature mainly originates from the K and K' points and contributes negligibly from the Γ point, applying an electric field in the plane of the sample activates three different transport paths. These findings suggest that the noncentrosymmetric version of the Kane-Mele family [i.e., $X_4YY'Z_6/X_4Y_2(ZZ')_3$] has the potential to enable novel physical phenomena and applications, including information transmission with multiple transport paths. For more information, refer to the SM [34].

VIII. HEXAGONAL TRIGONAL WARPING EFFECTS AND VALLEY SPIN VALVE EFFECT

To visualize the spin texture around the valley points and the morphology of the Fermi surface, we calculate constant-energy contour maps in the momentum space for different spin components, namely, S_x, S_y, and S_z. The results of this analysis are shown in Figs. 6(c) and 6(d). We observe that the constant-energy contours have distinct shapes around different high-symmetry k points in the Brillouin zone. Specifically, near the valley points (K and K'), the contours have a triangular shape, indicating a hexagonal warping character (as shown in Figs. 6(c) and 6(d) and described in the SM [34]) in the noncentrosymmetric version of the Kane-Mele $X_4Y_2Z_6$.

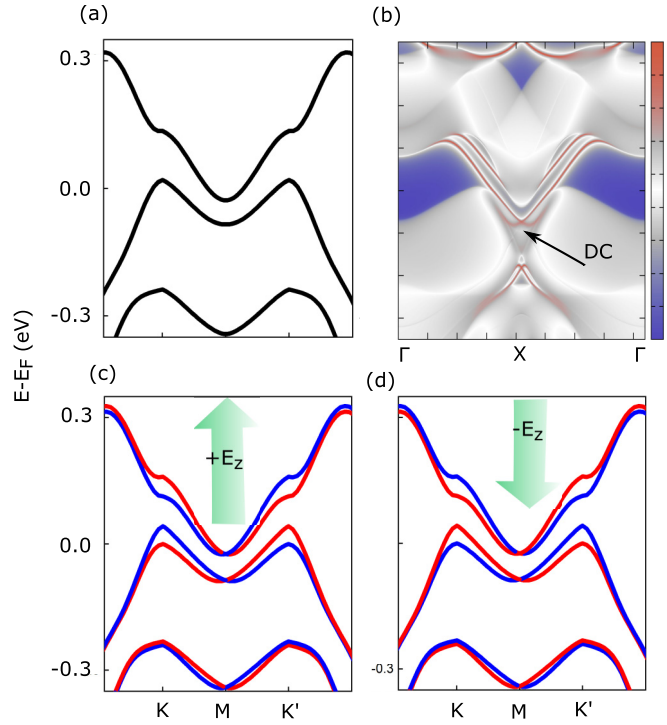

FIG. 7. (a) SOC-included energy spectrum and (b) corresponding surface state profile of the $(PtPd)_2Hg_2Se_6$ layer. The presence of a Dirac point signifies the robust topology in the $(PtPd)_2Hg_2Se_6$ layer. The SOC-included energy spectrum with (c) $+E_z = 0.3$ V/Å and (d) $-E_z = 0.3$ V/Å. The interchange of spin polarization between valleys K and K' makes the $(PtPd)_2Hg_2Se_6$-type layer useful for the valley spin valve effect.

Figure 7 illustrates that the spin and valley polarizations in the $(PtPd)_2HgSe_3$ and $(PtNi)_2HgSe_3$ layers are linked to the electric field orientation (it is either $+E_z$ or $-E_z$). By changing the direction of E_z, the polarization can be turned on or off, enabling the layers to serve as either a valley spin polarizer or a valley spin analyzer. This behavior can be exploited to create a functional device based on the valley spin valve effect. Such a device can switch conductance between an on or off state by adjusting the relative valley spin polarization established by the polarizer and analyzer.

IX. EFFECT OF EXTERNAL PERTURBATIONS

The topological properties of the proposed monolayers can be effectively tuned by external means such as exposing them to a vertical electric field or applying epitaxial strain engineering because the U value is sensitive to these external perturbations, allowing control over the resultant topological phase. As discussed above, the structural design Kane-Mele monolayers can be manipulated to disrupt centrosymmetry and alter their topological nature. This leads to the loss of Z_2 characteristics

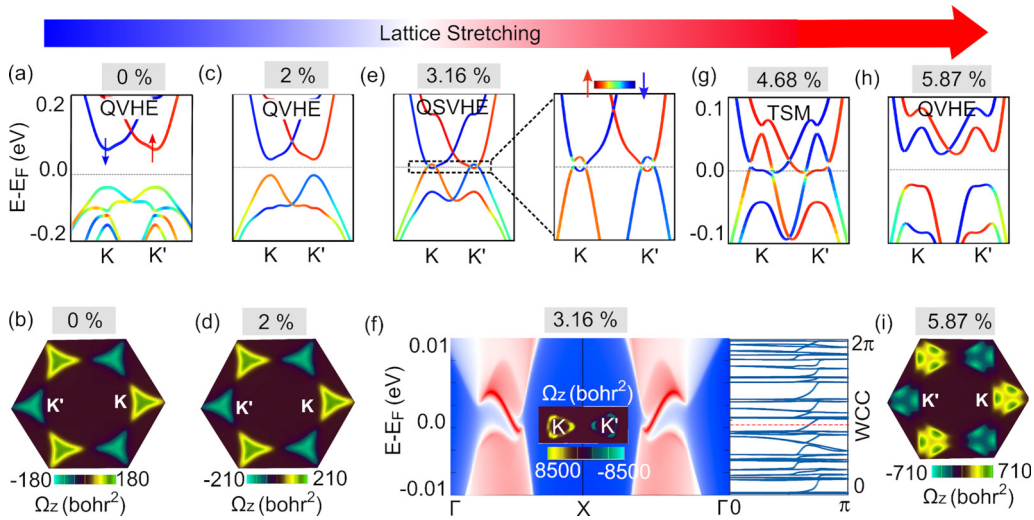

FIG. 8. Top: Evolution of the S_z-resolved energy spectrum of the $Pt_4Hg_2(SeTe)_3$ layer under various amounts of stretching. Band gap closing and reopening occur as the stretching increases, signifying a topological phase transition from QVH to QSH and again to the QVH state. Bottom: Corresponding Berry curvature, surface states, and Wannier charge center profiles.

in the Kane-Mele $X_4Y_2Z_6$ family, and a phase transition occurs from the Kane-Mele quantum spin Hall insulating phase to a quantum valley Hall phase (see Fig. 5 and Table I).

However, external methods such as epitaxial biaxial stretching can restore these noncentrosymmetric monolayers to the quantum spin Hall regime. For example, stretching the $Pt_4Hg_2(TeSe)_3$ layer to various degrees led to a decrease in the global band gap size as the U value decreased. At around 3.8% stretching, a topological phase transition occurred, resulting in the system becoming a Z_2 topological insulator (see Fig. 8). At this point, the $Pt_4Hg_2(TeSe)_3$ system also exhibited the QVH state, leading to the coexistence of quantum spin Hall and quantum valley Hall phases [Figs. 8(e) and 8(f)]. However, further stretching resulted in the system transitioning to topological semimetallic phases [Figs. 8(g) and 8(h)] and eventually returning to the quantum valley Hall phase [Fig. 8(g)]. These observations are completely consistent with our low-energy $k \cdot p$ model as presented in Fig. 1. Thus, an interesting topological phase diagram is achieved by subjecting the proposed monolayers to epitaxial strain. These noncentrosymmetric solids can be easily stretched through epitaxial growth over a suitable substrate with lattice mismatch, allowing them to realize multiple phases upon stretching.

The evaluation of the band structure for $Pt_4Hg_2(SSe)_3$ and $Pt_4Hg_2(TeSe)_3$ systems under different amounts of strain is demonstrated in Fig. S4 [34]. As can be seen, the stretching of these monolayers reduces the U values and hence reduces the global band gap at the K and K' points (see Fig. S4 [34]). Conversely, compressing these monolayers results in (1) an increase in the direct band gap and (2) a change in the nature of the global band gap from direct to indirect, with the conduction band minimum (CBM) shifting from the K or K' point to the Γ point (see [34]).

Parameters like global band gap and spin splitting size in our proposed monolayers can also be tuned by applying a vertical electric field because the U value is sensitive to the electric field orientation (see Fig. 9). However, the response to the electric field varies depending on the monolayer's chemical composition. For instance, applying a $+E_z$ $(-E_z)$ field to $Pt_4Hg_2(SSe)_3$ and $Pt_4Hg_2(STe)_3$ monolayers increases (decreases) the global band gap [see Figs. 9(a)–9(f)], while the effect is reversed in $Pt_4Hg_2(SeTe)_3$ [see Figs. 9(g)–9(i)]. This

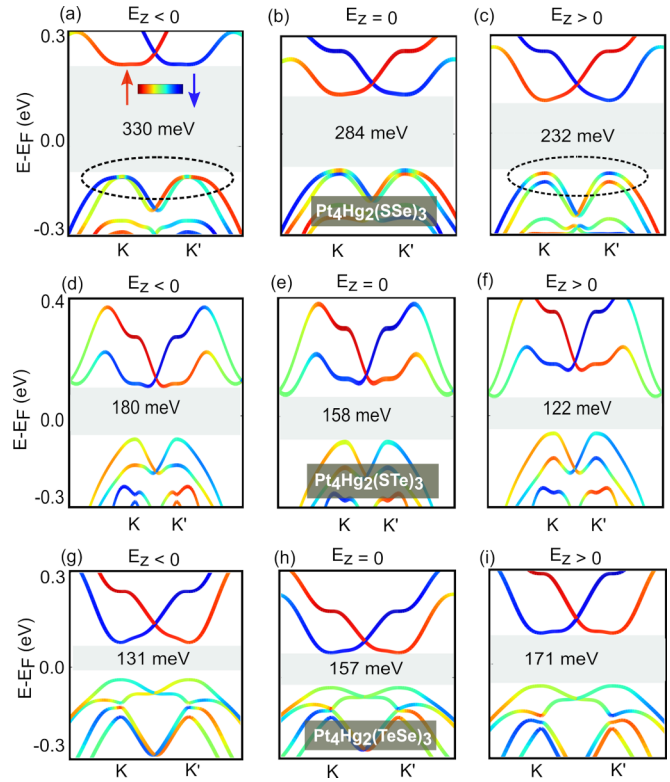

FIG. 9. Evolution of the S_z-resolved band structure for the (a)–(c) $Pt_4Hg_2(SSe)_3$, (d)–(f) $Pt_4Hg_2(STe)_3$, and (g)–(i) $Pt_4Hg_2(SeTe)_3$ layers under the electric field orientations $E_z < 0$ left), $E_z = 0$ (middle), and $E_z > 0$ (right). The strength of the electric field was chosen to be 0.3, 0.35, and 0.2 eV/Å in (a)–(f), (g). and (i). respectively. The sizes of the global band gap are highlighted in each plot.

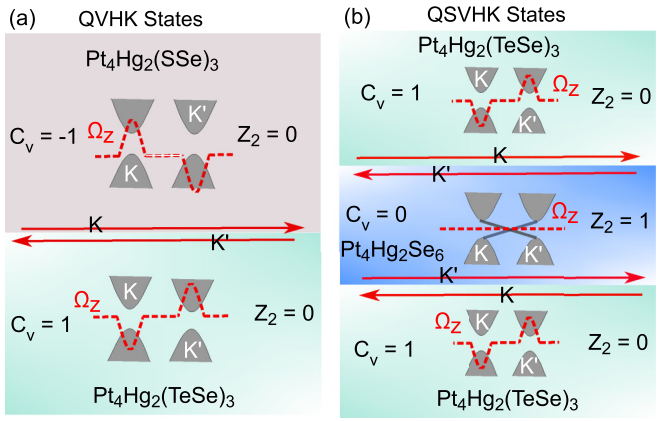

FIG. 10. (a) Realization of a quantum valley Hall kink (QVHK) state at the interface between the $Pt_4Hg_2(SSe)_3$ and $Pt_4Hg_2(TeSe)_3$ monolayers. (b) Realization of quantum spin-valley Hall kink (QSVHK) states at the interface between $Pt_4Hg_2(TeSe)_3$ and $Pt_4Hg_2Se_6$.

divergence in responses is due to opposing induced polarization in $Pt_4Hg_2(SeTe)_3$ and $Pt_4Hg_2(STe)_3STe$ monolayers. In addition, strengthening the $-E_z$ field in $Pt_4Hg_2(STe)_3$ monolayers moves the CBM from the Γ point to the K or K' point and converts the global band gap nature from indirect to direct [see Fig. 9(d)]. Meanwhile, increasing the strength of the $+E_z$ field in SSe noncentrosymmetric monolayers enhances the spin splitting in the valence bands. These findings show the potential for precise manipulation of band structure and spin properties in our proposed noncentrosymmetric monolayers through external electric fields.

X. QUANTUM SPIN-VALLEY HALL KINK STATES

The occurrence of kink states or zero line modes can be observed when there is an interface established between dissimilar topological phases. In particular, connecting two QVH insulators with different valley Chern numbers can lead to the manifestation of valley Hall kink states. Additionally, an interface between QSH and QVH insulators can result in the emergence of spin-valley Hall kink states at the interface boundary.

To realize QVH kink states, a domain wall is created between $Pt_4Hg_2(SSe)_3$ and $Pt_4Hg_2(STe)_3$ [or $Pt_4Hg_2(TeSe)_3$] due to the opposite Berry curvature of these materials (see Fig. 5). The schematic diagram in Fig. 10(a) illustrates the transition from the top, where QVH states with a valley Chern number of $C_v = -1$ exist, to the bottom, where QVH states also exist, but with the opposite Chern number of $C_v = 1$. At the interface, pure valley zero line modes could arise which support dissipationless pure valley currents that remain robust against valley-conservation scattering [see Fig. 10(a)].

Similarly, inserting $Pt_4Hg_2Se_6$, a Z_2 topological insulator, between two QVH insulators $Pt_4Hg_2(TeSe)_3$ [see Fig. 10(b)] can lead to the establishment of spin-polarized valley kink states across the interface, resulting in the realization of spin-valley helical kink states. These states can sustain a spin-valley-dependent current at the interface, which remains immune to spin-independent scattering and long-range intravalley scattering. The recent report on the spin-valley helical kink states in bismuthene by alloy engineering confirmed the potential of this approach [47].

XI. CONCLUSION

The noncentrosymmetric version of the Kane-Mele $X_4Y_2Z_6$ family, consisting of over 16 experimentally accessible members, was discovered in this study. The presence of larger SOC effects in this family compared to traditional Xene solids opens up opportunities for realizing the Kane-Mele model. By exploring these materials, a range of concurrent phenomena based on topology, spin, and valley degrees of freedom were identified.

These phenomena include the quantum valley and spin Hall effects and their coexistence, spin-valley locking, spin-valley selective optical interband transitions, the coexistence of Rashba and Ising spin splittings, valley spin valve functionality, and trigonal effects. Additionally, significant out-of-plane spontaneous electric polarization was observed in the proposed monolayers due to their noncentrosymmetry, with the magnitude varying based on the monolayers' chemical composition and electronegativity differences.

Moreover, the $X_4YY'Z_6/X_4Y_2(ZZ')_3$ monolayers have the potential to realize quantum valley Hall kink states when they interface due to their opposite Berry curvatures. Furthermore, various topological phase transitions among different phases can be achieved through external means such as applying a vertical electric field or stretching these noncentrosymmetric monolayers.

In conclusion, this study establishes a foundation for investigating spin-valley physics in low-dimensional topological materials with noncentrosymmetry. The noncentrosymmetric $X_4YY'Z_6/X_4Y_2(ZZ')_3$ Kane-Mele family exhibits a rich spectrum of phenomena and offers exciting prospects for spintronics and valleytronics applications.

ACKNOWLEDGMENTS

This work was financially supported by the National Natural Science Foundation of China (Grant No. 12350410367), the Foreign Expert Program-National Foreign Youth Talent Program of the Ministry of Science and Technology of China (Grant No. QN2023030010L) and the Alliance of International Science Organizations (ANSO) (Grant No. ANSO-VF-2024-03).

[1] J. R. Schaibley, H. Yu, G. Clark, P. Rivera, J. S. Ross, K. L. Seyler, W. Yao, and X. Xu, Valleytronics in 2D materials, Nat. Rev. Mater. **1**, 16055 (2016).

[2] S. Sharma, P. Elliott, and S. Shallcross, THz induced giant spin and valley currents, Sci. Adv. **9**, eadf3673 (2023).

[3] B. Edwards, O. Dowinton, A. E. Hall, P. A. E. Murgatroyd, S. Buchberger, T. Antonelli, G.-R. Siemann, A. Rajan, E. A. Morales, A. Zivanovic, C. Bigi, R. V. Belosludov, C. M. Polley, D. Carbone, D. A. Mayoh, G. Balakrishnan, M. S. Bahramy, and P. D. C. King, Giant valley-Zeeman coupling in the

surface layer of an intercalated transition metal dichalcogenide, Nat. Mater. **22**, 459 (2023).

[4] T. Zhang, X. Xu, B. Huang, Y. Dai, and Y. Ma, 2D spontaneous valley polarization from inversion symmetric single-layer lattices, npj Comput. Mater. **8**, 64 (2022).

[5] L. Banszerus, S. Moller, C. Steiner, E. Icking, S. Trellenkamp, F. Lentz, K. Watanabe, T. Taniguchi, C. Volk, and C. Stampfer, Spin-valley coupling in single-electron bilayer graphene quantum dots, Nat. Commun. **12**, 5250 (2021).

[6] K. S. Novoselov, A. K. Geim, S. V. Morozov, D. Jiang, Y. Zhang, S. V. Dubonos, I. V. Grigorieva, and A. A. Firsov, Electric field effect in atomically thin carbon films, Science **306**, 666 (2004).

[7] A. Molle, J. Goldberger, M. Houssa, Y. Xu, S.-C. Zhang, and D. Akinwande, Buckled two-dimensional Xene sheets, Nat. Mater. **16**, 163 (2017).

[8] F. Pielnhofer, T. V. Menshchikova, I. P. Rusinov, A. Zeugner, I. Y. Sklyadneva, R. Heid, K.-P. Bohnen, P. Golub, A. I. Baranov, E. V. Chulkov, A. Pfitzner, M. Ruck, and A. Isaeva, Designing 3D topological insulators by 2D-Xene (X = Ge, Sn) sheet functionalization in GaGeTe-type structures, J. Mater. Chem. C **5**, 4752 (2017).

[9] A. Zhao and B. Wang, Two-dimensional graphene-like Xenes as potential topological materials, APL Mater. **8**, 030701 (2020).

[10] P. Hogl, T. Frank, K. Zollner, D. Kochan, M. Gmitra, and J. Fabian, Quantum anomalous Hall effects in graphene from proximity-induced uniform and staggered spin-orbit and exchange coupling, Phys. Rev. Lett. **124**, 136403 (2020).

[11] X. Zhai and Y. M. Blante, Spin-valley polarized quantum anomalous Hall effect and a valley-controlled half-metal in bilayer graphene, Phys. Rev. B **101**, 155425 (2020).

[12] M. U. Rehman and Z. Qiao, Assessment of bilayer silicene to probe as quantum spin and valley Hall effect, Eur. Phys. J. B **91**, 42 (2018).

[13] M. U. Rehman and A. A. Abid, Quantum spin Hall and quantum valley Hall effects in trilayer graphene and their topological structures, Chin. Phys. B **26**, 127304 (2017).

[14] Z. U. Rahman, M. U. Rehman, M. Kiani, and N. Ullah, Emergence of topological and spin valley hallmarks in buckled Xene bilayers, J. Phys. D **56**, 445303 (2023).

[15] X. Xu, W. Yao, D. Xiao, and T. F. Heinz, Spin and pseudospins in layered transition metal dichalcogenides, Nat. Phys. **10**, 343 (2014).

[16] C. M. Gilardoni, F. Hendriks, C. H. van der Wal, and M. H. D. Guimaraes, Symmetry and control of spin-scattering processes in two-dimensional transition metal dichalcogenides, Phys. Rev. B **103**, 115410 (2021).

[17] I. Zutic, J. Fabian, and S. Das Sarma, Spintronics: Fundamentals and applications, Rev. Mod. Phys. **76**, 323 (2004).

[18] D. Xiao, G.-B. Liu, W. Feng, X. Xu, and W. Yao, Coupled spin and valley physics in monolayers of MoS_2 and other group-VI dichalcogenides, Phys. Rev. Lett. **108**, 196802 (2012).

[19] M. U. Rehman and Z. Qiao, MX family: An efficient platform for topological spintronics based on Rashba and Zeeman-like spin splittings, J. Phys.: Condens. Matter **35**, 015001 (2023).

[20] C. L. Kane and E. J. Mele, Z_2 topological order and the quantum spin Hall effect, Phys. Rev. Lett. **95**, 146802 (2005).

[21] I. Cucchi, A. Marrazzo, E. Cappelli, S. Riccò, F.Y. Bruno, S. Lisi, M. Hoesch, T.K. Kim, C. Cacho, C. Besnard, E. Giannini, N. Marzari, M. Gibertini, F. Baumberger, and A. Tamai, Bulk and surface electronic structure of the dual-topology semimetal Pt_2HgSe_3, Phys. Rev. Lett. **124**, 106402 (2020).

[22] K. Kandrai, P. Vancsó, G. Kukucska, J. Koltai, G. Baranka, Á. Hoffmann, Á. Pekker, K. Kamarás, Z. E. Horváth, A. Vymazalová, L. Tapasztó, and P. Nemes-Incze, Signature of large-gap quantum spin Hall state in the layered mineral jacutingaite, Nano Lett. **20**, 5207 (2020).

[23] A. Marrazzo, M. Gibertini, D. Campi, N. Mounet, and N. Marzari, Relative abundance of Z_2 topological order in exfoliable two-dimensional insulators, Nano Lett. **19**, 8431 (2019).

[24] R. Longuinhos, A. Vymazalova, A. R. Cabral, and J. Ribeiro-Soares, Raman spectrum of layered tilkerodeite (Pd_2HgSe_3) topological insulator: The palladium analogue of jacutingaite (Pt_2HgSe_3), J. Phys.: Condens. Matter **33**, 065401 (2021).

[25] A. Marrazzo, M. Gibertini, D. Campi, N. Mounet, and N. Marzari, Prediction of a large-gap and switchable Kane-Mele quantum spin Hall insulator, Phys. Rev. Lett. **120**, 117701 (2018).

[26] M. U. Rehman, M. Kiani, and J. Wang, Jacutingaite family: An efficient platform for coexistence of spin valley Hall effects, valley spin-valve realization, and layer spin crossover, Phys. Rev. B **105**, 195439 (2022).

[27] Z. Liu, Y. Han, Y. Ren, Q. Niu, and Z. Qiao, Van der Waals heterostructure Pt_2HgSe_3/CrI_3 for topological valleytronics, Phys. Rev. B **104**, L121403 (2021).

[28] M. U. Rehman, Z. Qiao, and J. Wang, Valley-symmetry-broken magnetic topological responses in $(Pt/Pd)_2HgSe_3/CrGeTe_3$ and Pd_2HgSe_3/CrI_3 through interfacial coupling, Phys. Rev. B **105**, 165417 (2022).

[29] P. E. Blochl, Projector augmented-wave method, Phys. Rev. B **50**, 17953 (1994).

[30] G. Kresse and J. Furthmuller, Efficient iterative schemes for *ab initio* total-energy calculations using a plane-wave basis set, Phys. Rev. B **54**, 11169 (1996).

[31] A. A. Mostofi, J. R. Yates, Y.-S. Lee, I. Souza, D. Vanderbilt, and N. Marzari, wannier90: A tool for obtaining maximally-localised Wannier functions, Comput. Phys. Commun. **178**, 685 (2008).

[32] G. Pizzi, V. Vitale, R. Arita, S. Blügel, F. Freimuth, G. Géranton, M. Gibertini, D. Gresch, C. Johnson, T. Koretsune, J. Ibañez-Azpiroz, H. Lee, J.-M. Lihm, D. Marchand, A. Marrazzo, Y. Mokrousov, J. I Mustafa, Y. Nohara, Y. Nomura, L. Paulatto *et al.*, Wannier90 as a community code: New features and applications, J. Phys.: Condens. Matter **32**, 165902 (2020).

[33] Q. Wu, S. Zhang, H.-F. Song. M. Troyer, and A. A. Soluyanov, WannierTools: An open-source software package for novel topological materials, Comput. Phys. Commun. **224**, 405 (2018).

[34] See Supplemental Material at http://link.aps.org/supplemental/10.1103/PhysRevB.109.165424 for detailed computational methods, spin-resolved band structures, and electrostatic potential profiles across the layers for various members of the $X_4YY'Z_6/X_4Y_2(ZZ')_3$ family, which includes Refs. [22,24,29–33,43–46].

[35] Z. Qiao, W.-K. Tse, H. Jiang, Y. Yao, and Q. Niu, Two-dimensional topological insulator state and topological phase transition in bilayer graphene, Phys. Rev. Lett. **107**, 256801 (2011).

[36] Z. Qiao, H. Jiang, X. Li, Y. Yao, and Q. Niu, Microscopic theory of quantum anomalous Hall effect in graphene, Phys. Rev. B **85**, 115439 (2012).

[37] V. Vargiamidis, P. Vasilopoulos, and N. Neophytou, Tunable topological phases in monolayer Pt_2HgSe_3 with exchange fields, Phys. Rev. B **106**, 205416 (2022).

[38] M. U. Rehman, X. Dong, T. Hou, Z. Li, S. Qi, and Z. Qiao, Quantum anomalous Hall effect by coupling heavy atomic layers with CrI_3, Phys. Rev. B **100**, 195422 (2019).

[39] C. W. Jang, W. J. Lee, J. K. Kim, S. M. Park, S. Kim, and S.-H. Choi, Growth of two-dimensional Janus MoSSe by a single in situ process without initial or follow-up treatments, NPG Asia Mater. **14**, 15 (2022).

[40] R. Sant, M. Gay, A. Marty, S. Lisi, R. Harrabi, C. Vergnaud, M. T. Dau, X. Weng, J. Coraux, N. Gauthier, O. Renault, G. Renaud, and M. Jamet, Synthesis of epitaxial monolayer Janus SPtSe, npj 2D Mater. Appl. **4**, 41 (2020).

[41] X. Wan, E. Chen, J. Yao, M. Gao, X. Miao, S. Wang, Y. Gu, S. Xiao, R. Zhan, K. Chen, Z. Chen, X. Zeng, X. Gu, and J. Xu, Synthesis and characterization of metallic Janus MoSH monolayer, ACS Nano **15**, 20319 (2021).

[42] G. Hussain, A. Samad, and M. U. Rehman, Emergence of Rashba splitting and spin-valley properties in Janus $MoGeSiP_2As_2$ and $WGeSiP_2As_2$ monolayers, J. Magn. Magn. Mater. **563**, 169897 (2022).

[43] J. P. Perdew, J. A. Chevary, S. H. Vosko, K. A. Jackson, M. R. Pederson, D. J. Singh, and C. Fiolhais, Atoms, molecules, solids, and surfaces: Applications of the generalized gradient approximation for exchange and correlation, Phys. Rev. B **46**, 6671 (1992).

[44] A. Togo and I. Tanaka, First principles phonon calculations in materials science, Scr. Mater. **108**, 1 (2015).

[45] H.-J. Kim, VASPBERRY code, version V1.0, 2018, https://github.com/Infant83/VASPBERRY.

[46] U. Herath, P. Tavadze, X. He, E. Bousquet, S. Singh, F. Munoz, and A. H. Romero, PyProcar: A Python library for electronic structure pre/post-processing, Comput. Phys. Commun. **251**, 107080 (2020).

[47] T. Zhou, S. Cheng, M. Schleenvoigt, P. Schüffelgen, H. Jiang, Z. Yang, and I. Žutić, Quantum spin-valley Hall kink states: From concept to materials design, Phys. Rev. Lett. **127**, 116402 (2021).